





21

## Abstract

22 This study reveals that haze pollution (HP) over the North China Plain (NCP) in  
23 winter can persist to following spring during most years. The persistence of  $HP_{NCP}$  is  
24 attributed to maintenance of an anticyclonic anomaly (AA) over northeast Asia and  
25 southerly wind anomalies over the NCP. Southerly wind anomalies over the NCP  
26 reduce surface wind speed and increase relative humidity, which are conducive to  
27 above-normal  $HP_{NCP}$  both in winter and spring. However, there exist several years  
28 when above-normal  $HP_{NCP}$  in winter are followed by below-normal  $HP_{NCP}$  in the  
29 following spring. The reversed  $HP_{NCP}$  in winter and spring in these years is due to the  
30 inverted atmospheric anomalies over northeast Asia. In particular, AA over northeast  
31 Asia in winter is replaced by a cyclonic anomaly (CA) in the following spring. The  
32 resultant spring northerly wind anomalies over NCP are conducive to below-normal  
33  $HP_{NCP}$ . These two distinctive evolutions of  $HP_{NCP}$  and atmospheric anomalies over  
34 northeast Asia from winter to spring are attributed to the different evolutions of sea  
35 surface temperature anomalies (SSTA) in the North Atlantic. In the persistent years,  
36 warm North Atlantic SSTA in winter maintains to following spring via positive air-sea  
37 interaction process and induces a negative spring North Atlantic Oscillation  
38 (NAO)-like pattern, which contributes to the AA over northeast Asia via atmospheric  
39 wave train. By contrast, in the reverse years, cold SSTA in the North Atlantic is  
40 maintained from winter to spring, which induces a positive spring NAO-like pattern  
41 and leads to CA over northeast Asia via atmospheric wave train. The findings suggest  
42 that North Atlantic SSTA plays crucial roles in modulating the distinct evolutions of



43  $HP_{NCP}$  from winter to succedent spring, which can be served as an important  
44 preceding signal for haze pollution evolution over the North China Plain.

45 **Keywords:** Evolution of Haze pollution; North China Plain; North Atlantic sea  
46 surface temperature; North Atlantic Oscillation; Atmospheric circulation

47

48



## 49 1. Introduction

50 Haze pollution has become a serious air quality issue in China accompanying the  
51 rapid urbanization and fast economic development (e.g. Ding and Liu 2004; Wang  
52 and Chen 2016; Zhang et al. 2018). It has been well recognized that the occurrences  
53 of haze pollution event can exert substantial impacts on the human health, air  
54 transportation, ground traffic, agriculture production, and regional climate change (e.g.  
55 Koren et al. 2012; Zhang and Crooks 2012; Fu et al. 2014; Wang et al. 2014a, 2014b;  
56 Wu et al. 2016; Tie et al. 2016; Cohen et al. 2017; Guo et al. 2018; Zhang et al. 2018;  
57 Lu et al. 2019). For example, Cohen et al. (2017) reported that near 4.2 million  
58 premature deaths in the world in 2015 were attributed to the overexposure of PM<sub>2.5</sub>.  
59 In addition, haze pollution is suggested to result in a decrease of about 1.2%-3.8% of  
60 the annual Gross National Product (GNP, Zhang and Crooks 2012). Furthermore,  
61 increasing concentration of anthropogenic aerosol, which is related to the enhanced  
62 haze pollution, could exert significant impacts on the atmospheric circulation and  
63 regional precipitation change (Koren et al. 2012; Wang et al. 2014). Considering the  
64 notable impacts of haze pollution, it is of great scientific importance to improve our  
65 understanding of the factors contributing to haze pollution and the associated  
66 mechanisms.

67 A number of previous studies have investigated the factors responsible for the  
68 variations of haze pollution in China on multiple timescales. The long-term increasing  
69 trend of haze pollution in China is generally attributable to the rapid increases in  
70 anthropogenic emissions (e.g. Che et al. 2009; Ding and Liu 2014; Zhao et al. 2016;



71 Cheng et al. 2019). For example, Zhao et al. (2016) showed that the notable  
72 increasing trend of haze pollution in winter over eastern China has a close relationship  
73 with the Gross Domestic Product (GDP) in China. Several studies suggested that  
74 changes in the meteorological conditions due to global warming also play a role in the  
75 long-term trend of haze pollution in China (e.g. Cai et al. 2017; Liu et al. 2017; Ding  
76 et al. 2017; Zhang et al. 2020).

77 On the interannual and interdecadal timescales, variations of the haze pollution  
78 in China are suggested to be mainly controlled by the meteorological conditions. For  
79 instance, Dang and Liao (2019) reported that the changes of meteorological  
80 conditions accounted for about 70% of the variation of the annual haze days in the  
81 Beijing-Tianjin-Hebei region. Zhao et al. (2016) suggested that the Pacific Decadal  
82 Oscillation could exert marked impacts on the interdecadal variation of the haze  
83 pollution in eastern China via inducing large-scale atmospheric circulation anomalies  
84 over East Asia. Pacific Decadal Oscillation is the first leading mode of sea surface  
85 temperature anomalies (SSTA) in the North Pacific on the interdecadal timescale  
86 (Mantua et al., 1997; Zhang et al., 1997; Duan et al. 2013). Xiao et al. (2014) showed  
87 that the Atlantic Multidecadal Oscillation modulates haze pollution in China via  
88 triggering atmospheric wave train over Eurasia. Atlantic Multidecadal Oscillation is  
89 the dominant mode of SSTA in the North Atlantic on the multidecadal timescale (Kerr  
90 2000). Compared to the interdecadal variation, much more studies have examined the  
91 factors for the interannual variation of haze pollution in China, mainly concentrating  
92 on boreal winter. It is shown that interannual variation of haze pollution in eastern



93 China can be impacted by the Arctic Oscillation (Yin et al. 2015), East Asian winter  
94 Monsoon (Li et al. 2016; Chen et al. 2020), El Niño-Southern Oscillation (Guo and Li  
95 2015; Chang et al. 2016; Liu et al. 2017; Li et al. 2017; He et al. 2019), North Atlantic  
96 SSTA (Xiao et al. 2014), Arctic sea ice (Wang et al. 2015; Yin and Wang 2017),  
97 Eurasian snow cover (Yin and Wang 2018), and the East Atlantic-Western Russian  
98 (EAWR) teleconnection pattern (Yin and Wang 2017; Chen et al. 2020). A recent  
99 study has examined the factors modulating the interannual variation of springtime  
100 haze pollution in the North China Plain Region (NCPR) (Chen et al. 2019). Note that  
101 NCPR is one of the most important regions in China with very dense population, large  
102 traffic activities and highly developed economy. In addition, NCPR is also the most  
103 polluted region in China (Yin et al. 2015). Chen et al. (2019) indicated that North  
104 Atlantic SSTA and the North Atlantic Oscillation (NAO, the first leading mode of  
105 interannual atmospheric variability over the North Atlantic region; Hurrell 1995) play  
106 important roles in determining the haze pollution over NCPR via modulating  
107 atmospheric circulation anomalies over northeast Asia through triggering atmospheric  
108 wave train extending from North Atlantic across Europe to East Asia (Chen et al.  
109 2019). Previous studies mainly investigated interannual variations of haze pollution  
110 over the NCPR in winter and spring separately. However, impacts of haze pollution  
111 may depend strongly on the time period of persistence. Hence, an important question  
112 is raised: whether there exists a relation between interannual variation of haze  
113 pollution over the NCPR in winter and following spring? In particular, could the  
114 wintertime haze pollution maintain from winter to the following spring? If so, what



115 are the plausible factors contributing to the across-season persistence of haze  
116 pollution over the NCPR from winter to succedent spring? Understanding the  
117 evolution features of the haze pollution from winter to spring and the associated  
118 mechanisms would have important implications for the seasonal prediction of haze  
119 pollution over the NCPR. In this study, the issues raised above will be investigated  
120 and addressed.

121 The remainder of this paper is organized as follows. Section 2 describes the data  
122 and methods used in this study. Section 3 examines relation of interannual variations  
123 between winter and spring haze pollution over the NCPR, and compares the two  
124 distinct types of haze evolutions found in this paper. Section 4 examines the factors  
125 responsible for the different evolutions of haze pollution over NCPR from winter to  
126 the following spring. Summary and discussion are provided in section 5.

127

## 128 **2. Data and methods**

### 129 **2.1 Data**

130 Monthly mean horizontal winds, geopotential height, relative humidity, surface  
131 wind speed, surface heat fluxes are obtained from the National Centers for  
132 Environmental Prediction-National Center for Atmospheric Research (NCEP-NCAR)  
133 reanalysis (Kalnay et al. 1996;  
134 <https://psl.noaa.gov/data/gridded/data.ncep.reanalysis.html>), which are available from  
135 January 1948 to the present. Surface heat fluxes are the sum of the surface latent and  
136 sensible heat fluxes, surface shortwave and longwave radiations. Atmospheric data



137 from the NCEP-NCAR reanalysis have a horizontal resolution of  $2.5^{\circ} \times 2.5^{\circ}$  in the  
138 longitude-latitude grids, while surface heat fluxes are on T62 Gaussian grids. Monthly  
139 mean SST data are derived from the National Oceanic and Atmospheric  
140 Administration (NOAA) Extended Reconstructed SST version 5 (ERSSTV5) from  
141 January 1854 to the present (Huang et al. 2017;  
142 <https://psl.noaa.gov/data/gridded/data.noaa.ersst.v5.html>), with a horizontal resolution  
143 of  $2^{\circ} \times 2^{\circ}$  in the longitude-latitude grids. Atmospheric teleconnection indices,  
144 including the EAWR index and NAO index, are provided by the NOAA Climate  
145 Prediction Center (<https://www.cpc.ncep.noaa.gov/data/>).

146 Surface data of visibility and relative humidity observed at 748 meteorological  
147 stations are extracted from the National Meteorological Information Center of China  
148 from 1979 to 2012. These meteorological observations are measured daily at 0200,  
149 0800, 1400 and 2000 Beijing time (UTC+8). Following previous studies (Guo et al.  
150 2017; Chen et al. 2019, 2020), a series of quality control techniques are applied to this  
151 meteorological data to ensure its quality and consistency. In particular, we exclude the  
152 observation station if it contains any missing values throughout the whole analysis  
153 period. In addition, the data has been removed when precipitation, snow events, and  
154 dust storms occurred. After the above quality control, there remain 218 stations over  
155 Eastern China (Fig. 1a). Furthermore, following previous studies (Che et al. 2009;  
156 Guo et al. 2017, Chen et al. 2019; 2020), we only use the data at 1400 Beijing time, as  
157 this time may be the most representative of the daily visibility compared to other  
158 times. It should be mentioned that the atmospheric visibility, which is traditionally





159 measured by human visual observation, starts to be determined by the automatic  
160 visibility instruments since the year 2014. Due to the changes of the observation  
161 methods, large uncertainties have emerged due to the issues of heterogeneity as  
162 reported by Li et al. (2018). Thus, this study does not employ the visibility data after  
163 the 2014.

164 Long-term trends of all variables have been removed to avoid the impact of the  
165 global warming signal and to focus on the interannual variation of haze pollution.  
166 Anomalies are calculated by subtracting the monthly climatology from the original  
167 data. Significance levels of correlation coefficient and composite differences are  
168 estimated based on the two-tailed Student's *t* test.

169

## 170 **2.2 Dry Extinction coefficient of aerosol**

171 As in previous studies (Li et al. 2018; Guo et al. 2017; Chen et al. 2019, 2020),  
172 this study employs the dry extinction coefficient (DECC) of aerosol to represent the  
173 haze pollution. The DECC is defined based on the Koschmieder relationship  
174 (Koschmieder 1926):

$$175 \quad DECC = \frac{K}{Vis_{dry}} \quad (1)$$

176 where *K* is equal to 3.912, *Vis<sub>dry</sub>* indicates atmospheric visibility after removing the  
177 effect of relative humidity. It is noted that atmospheric visibility is not only impacted  
178 by the dry particles, but also affected by the amount of water uptake. For instance,  
179 high humidity associated with fog could lead to reduction of atmospheric visibility.  
180 Previous studies suggested that the visibility needs to be corrected in the presence of a



181 relative humidity ranging from 40 to 90% (e.g. Rosenfeld et al. 2007), which is  
182 expressed as follows:

$$183 \quad Vis_{dry} = \frac{Vis_{obs}}{0.26 + 0.4285 \log(100 - RH)} \quad (2)$$

184 where  $Vis_{obs}$  indicates the observed visibility. Note that all visibility data are discarded  
185 when the relative humidity (RH) is higher than 90% to remove the influence of fog  
186 events, non-linear aerosol and water interactions (Craig and Faulkenberry 1979; Guo  
187 et al. 2017; Chen et al. 2019, 2020).

188

### 189 *2.3 Wave activity flux*

190 We use the wave activity flux defined by Takaya and Nakamura (2001) to  
191 examine the stationary Rossby wave propagation, which can be expressed as follows:

$$192 \quad W = \frac{1}{2|U|} \begin{pmatrix} U(v'^2 - \psi' v'_x) + V(-u' v' + \psi' u'_x) \\ U(-u' v' + \psi' u'_x) + V(u'^2 + \psi' u'_y) \\ \frac{f_0 R_a p}{N^2 H_0} \left\{ U(v' T' - \psi' T'_x) + V(-u' T' - \psi' T'_y) \right\} \end{pmatrix} \quad (3)$$

193 where  $\mathbf{U} = (U, V)$  is the climatological wind vector.  $\mathbf{V} = (u', v')$  denotes  
194 geostrophic winds anomalies.  $\psi'$  is geostrophic stream function anomalies.  $H_0$ ,  $p$ ,  
195 and  $N$  represent scale height, pressure normalized by 1000-hPa, and Brunt-Vaisala  
196 frequency, respectively.  $R_a$ ,  $T'$ , and  $f_0$  denote gas constant of the dry air, air  
197 temperature anomalies, and the Coriolis parameter at 45°N, respectively. Subscripts x  
198 and y are the derivatives in the zonal and meridional directions, respectively.  
199 Climatological mean is calculated over the 1980–2010 period.

200



## 201 **2.4 Barotropic model**

202 The present study employs a linear barotropic model to investigate the role of the  
203 SST anomalies (SSTA) over the subtropical and tropical North Atlantic in triggering  
204 atmospheric Rossby wave train over mid-high latitudes of Eurasia. Previous studies  
205 have demonstrated that cold (warm) SSTA in the subtropical and tropical regions are  
206 able to induce convergence (divergence) anomalies at the upper-troposphere that act  
207 as effective sources of atmospheric stationary Rossby wave (Hodson et al. 2010;  
208 Watanabe 2004; Zuo et al. 2013; Wu et al. 2011; Chen et al. 2016, 2020). Based on a  
209 simple barotropic vorticity equation (Watanabe 2004; Sardeshmukh and Hoskins 1988;  
210 Chen et al. 2020), the barotropic model is established by:

$$211 \quad \partial_t \nabla^2 \psi' + J(\bar{\psi}, \nabla^2 \psi') + J(\psi', \nabla^2 \bar{\psi} + f) + \alpha \nabla^2 \psi' + \nu \nabla^6 \psi' = S' \quad (4)$$

212 where  $\psi'$  and  $\bar{\psi}$  are the perturbation stream function and basic state stream  
213 function, respectively.  $f$  and  $J$  represent the Coriolis parameter and Jacobian  
214 operator, respectively.  $S'$  represents the vorticity source generated by the atmospheric  
215 divergence. The barotropic model consists a biharmonic diffusion and a linear  
216 damping that indicate the Rayleigh friction. Note that solution of the above Equation  
217 associated with the barotropic model is determined by the vorticity perturbation ( $S'$ )  
218 and the basic state. In the present analysis, the basic state is chosen at the 300-hPa  
219 level over 1979-2010 using the NCEP-NCAR reanalysis data. O'Reilly et al. (2018)  
220 reported that results of the barotropic model experiments are insensitive to the basic  
221 states chosen from the upper troposphere (e.g., from 350-hPa to 200-hPa). It should  
222 be mentioned that the basic state is chosen from the upper troposphere because the



223 strongest convergence/divergence anomalies generated by the tropical and subtropical  
224 SST cooling/warming tend to be observed at the upper troposphere (e.g., Sun et al.  
225 2015; Krishnamurti et al. 2013; O'Reilly et al. 2018; Chen et al. 2020).

226

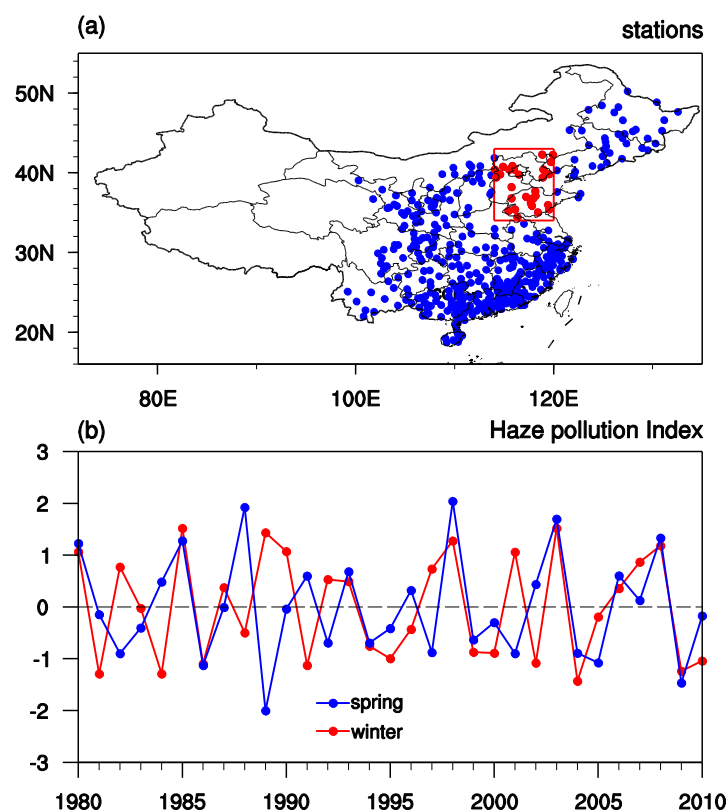
### 227 **3. Connection of haze pollution over NCPR in winter and spring**

228 Following previous analyses (Yin and Wang 2016; Chen et al. 2019, 2020), the  
229 NCPR corresponds to the region spanning  $34^{\circ}$ – $43^{\circ}$ N,  $114^{\circ}$ – $120^{\circ}$ E. Slight changes of  
230 the region to represent NCPR don't affect the main results of this study. Figure 1a  
231 shows that there are a total of 26 meteorological observational stations in the NCPR  
232 (red dots in the box). As in previous studies (Yin and Wang 2016; Chen et al. 2019,  
233 2020), this analysis defines a NCPR DECC index (NDI for short) by averaging the  
234 DECC anomalies over the above 26 stations to describe variation of haze pollution  
235 over the NCPR.

236 Figure 1b shows year-to-year variations of the NDI in winter and the following  
237 spring over 1980–2011. The correlation coefficient between the winter and spring  
238 NDI over 1980–2011 is 0.30, exceeding the 90% confidence level, which suggests a  
239 marginal in-phase variation of the haze pollution in winter and the following spring.  
240 In particular, most of the positive (negative) values of winter NDI are followed by  
241 extremely large (small) values of the spring NDI (for example, years in 1980, 1985,  
242 1986, etc.). This suggests that air condition over the NCPR in the following spring  
243 tends to be better (worse) than normal if haze pollution in preceding winter is less  
244 (more) serious over the NCPR. As shown in Fig. 1b, however, there also exists several



245 years when values of the winter and following spring NDI are strongly opposite,  
246 showing out-of-phase variation. In these years, large negative (positive) values of  
247 winter NDI are followed by large positive (negative) spring NDI (Fig. 1b). For  
248 instance, in 1984 and 1991, the winter NDIs are significantly negative, while the  
249 following spring NDIs are significantly positive. In 1982 and 1989, large positive  
250 values of winter NDI are followed by large negative values of spring NDI.



251  
252 **Figure 1.** (a) Geographical locations of the meteorological stations (denoted by dots)  
253 in China. Red dots represent the meteorological stations in the NCPR. (b)  
254 Standardized time series of the NDI in winter (December-January-February-mean,  
255 D(0)JF(1) for short) and its following spring (March-April-May-mean, MAM(1) for  
256 short) over 1980-2010.



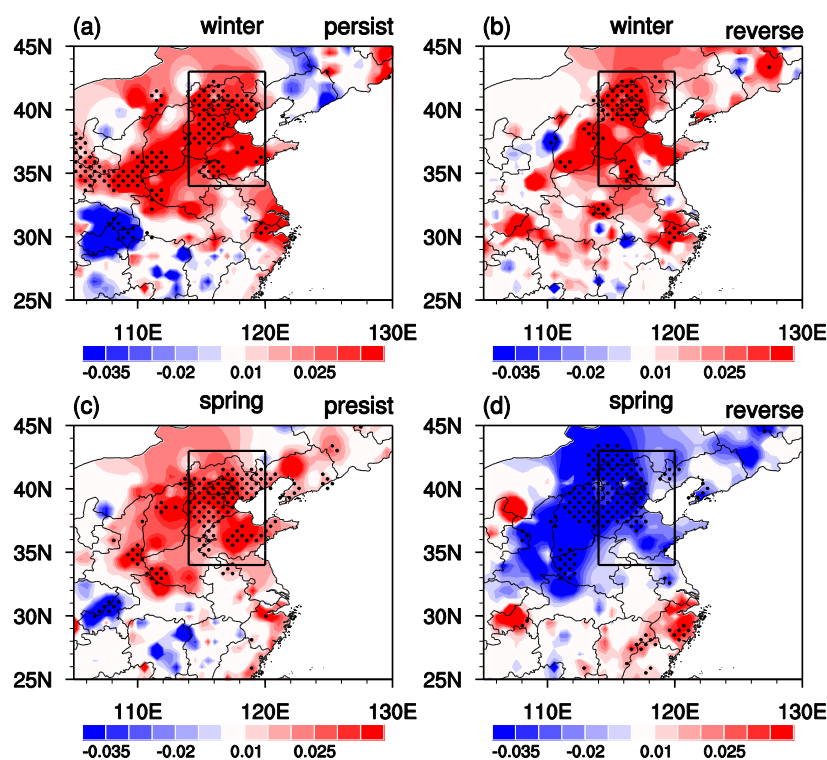
257 **Table 1.** Lists of the persistent and reverse years.

Persistence (11 years)	Reverse (9 years)
1980, 1985, 1986, 1993, 1994, 1998, 1999, 2003, 2004, 2008, 2009	1982, 1984, 1988, 1989, 1991, 1992, 1997, 2001, 2002

258 In the following, positive (negative) phases of the winter and spring NDIs are  
259 identified when the normalized NDIs are larger (less) than 0.43. Previous studies  
260 indicated that value of  $\pm 0.43$  standard deviation can separate a time series into three  
261 portions (positive and negative phases, and normal condition) with nearly the same  
262 sample sizes. Note that a use of  $\pm 0.5$  standard deviation as the threshold to define  
263 anomalous NDI years leads to similar results, but with smaller sample sizes. Table 1  
264 presents the years when winter and spring NDIs are in-phase and out-of-phase.  
265 According to Table 1, there are a total of 11 (9) years for the in-phase (out-of-phase).  
266 Relatively less number of out-of-phase years than in-phase years is found during  
267 1980–2011, in concert with the evidence that winter NDI has a marginal positive  
268 correlation with the spring NDI. In the following, out-of-phase (in-phase) years are  
269 called (reverse) persistent years for convenience of descriptions. We employ  
270 composite analysis to compare evolutions of DECC and atmospheric anomalies  
271 between the persistent and reverse years. Note that in performing the composite  
272 analysis, we reversed the anomalies when the winter NDI is negative since, to a large  
273 extent, the DECC and atmospheric circulation anomalies over the NCPR are  
274 symmetric between the positive and negative phases of the winter NDI. Hence, the  
275 descriptions below are corresponding to the positive phases of the winter NDI, but



276 also apply to the negative phases except with opposite signs.

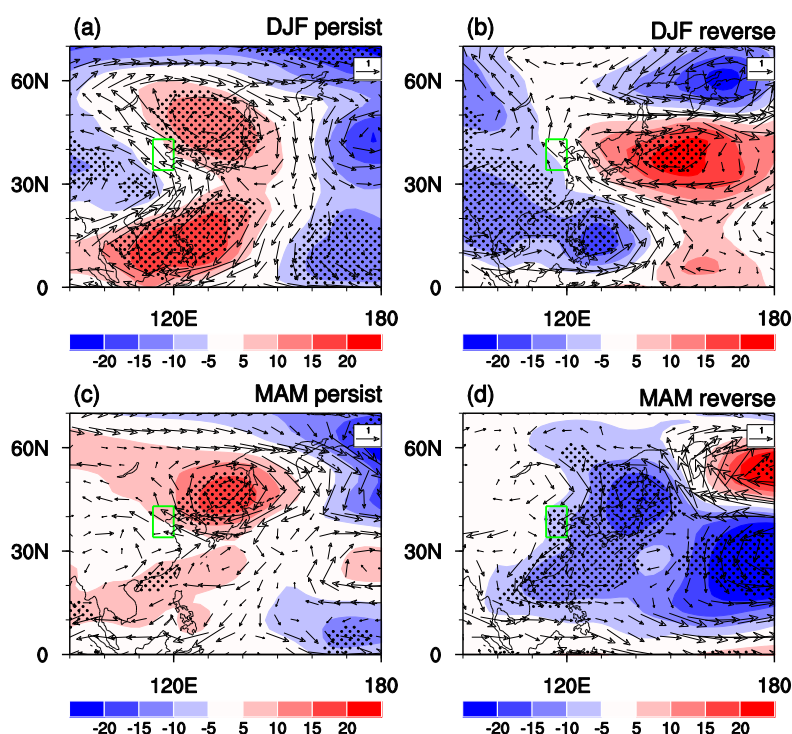


277  
278 **Figure 2.** Composite anomalies of DECC (unit:  $\text{km}^{-1}$ ) in (a, b) winter and (c, d) spring  
279 in the (left column) persistent years and the (right column) reverse years. Stippling  
280 regions indicate anomalies significant at the 5% level.

281 Figure 2 shows composite anomalies of DECC in winter and following spring in  
282 the persistent and reverse years. For the persistent years, large positive DECC  
283 anomalies (indicating more serious haze pollution) are seen over the NCP and  
284 surrounding regions (Fig. 2a). DECC anomalies in winter over southern China are  
285 weak, suggesting a weak relation of the haze pollution between northern and southern  
286 China, consistent with previous studies (e.g. Li et al. 2017; He et al. 2019). Large  
287 positive DECC anomalies over the NCP are maintained to the succedent spring with



288 comparable amplitude (Figs. 2a and 2c). For the reverse years, large positive DECC  
289 anomalies also appear over the NCPR in winter (Fig. 2b). However, in the following  
290 spring, the NCPR and surrounding regions are dominated by significantly negative  
291 values of DECC (Fig. 2d) (indicating air condition in spring becomes better), which is  
292 in sharp contrast to that for the persistent years (Fig. 2c).



293  
294 **Figure 3.** Composite anomalies of 850-hPa winds (vectors, unit:  $\text{m s}^{-1}$ ) and  
295 streamfunction (shadings; unit:  $10^5 \text{ m}^2 \text{ s}^{-1}$ ) in (a, b) winter and (c, d) spring in the (left  
296 column) persistent years and the (right column) reverse years. Stippling regions  
297 indicate streamfunction anomalies that are statistically significant at the 5% level.

298 Studies have demonstrated that meteorological conditions related to the  
299 atmospheric anomalies can explain above 66% of interannual and interdecadal  
300 variations of haze pollution over most parts of Eastern China (Zhang et al. 2014; Chen



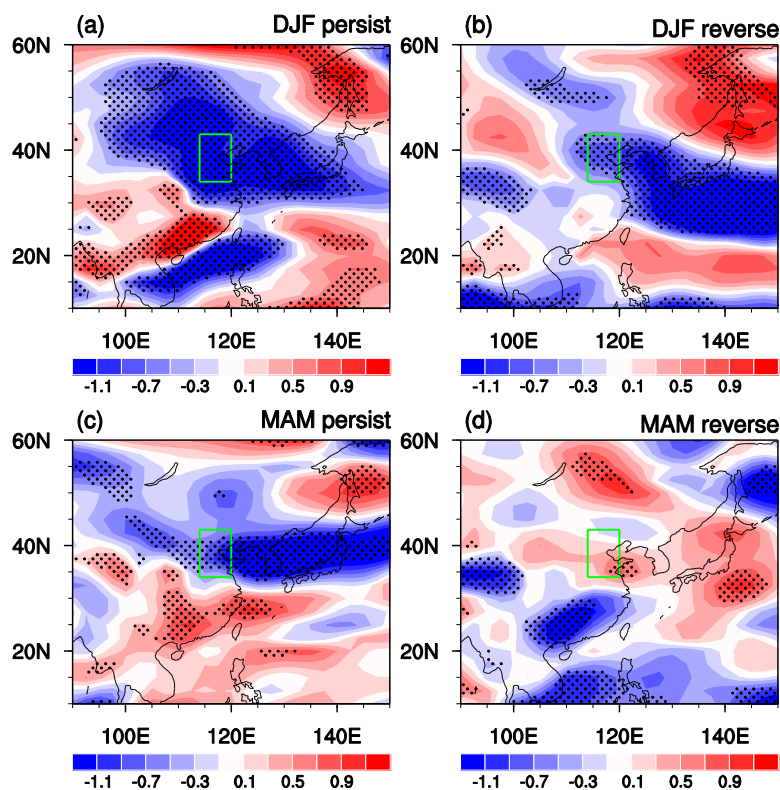


301 et al. 2019; He et al. 2019; Dang and Liao 2019; Ma and Zhang 2020). Hence, it is  
302 expected that different evolutions of the DECC anomalies from winter to following  
303 spring over the NCPR may be associated with the distinct evolutions of atmospheric  
304 anomalies. Composite anomalies of winds and streamfunction at 850hPa in winter and  
305 following spring for the persistent and reverse years are shown in Fig. 3. In the  
306 persistent years, a significant anticyclonic anomaly is seen over northeast Asia,  
307 accompanied by strong southerly winds anomalies over NCPR, and northerly wind  
308 anomalies over mid-latitudes North Pacific (Fig. 3a). In addition, another marked  
309 anticyclonic anomaly appears over south China sea and Philippine sea, leading to  
310 strong southerly wind anomalies over southern China (Fig. 3a). The anomalous  
311 anticyclone over northeast Asia and associated southerly wind anomalies over NCPR  
312 are maintained to following spring (Fig. 3c).

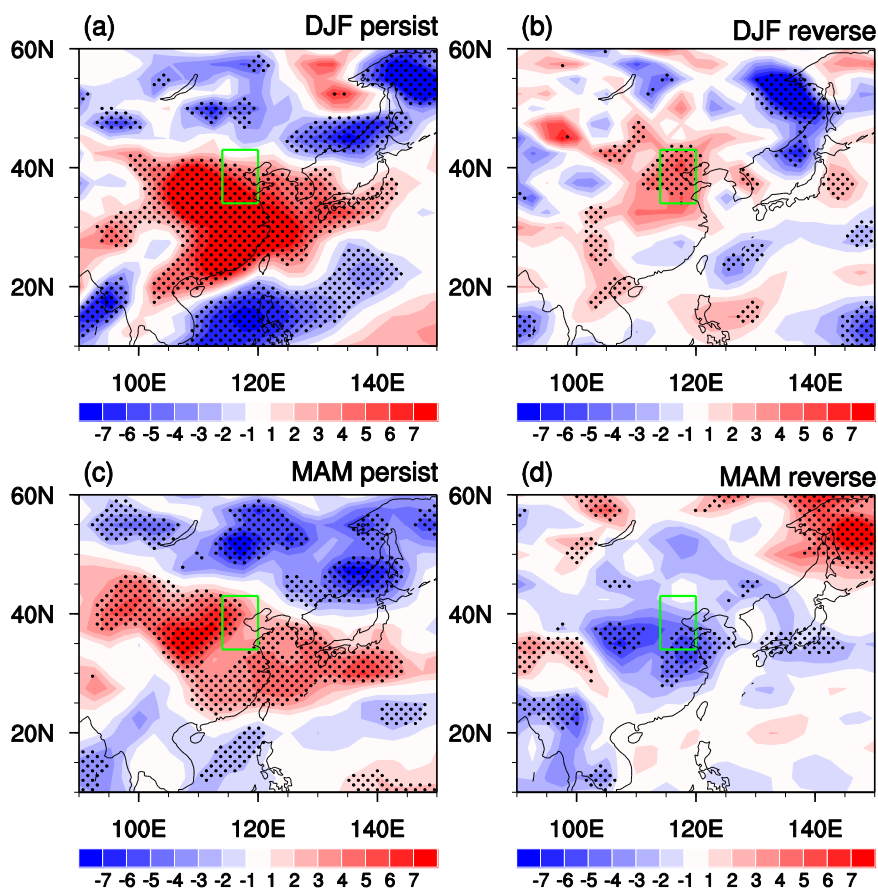
313 For the reverse years, a strong anticyclonic anomaly also exists over northeast  
314 Asia, but with a southeastward displacement (Fig. 3b) compared to that in the  
315 persistent years. Note that NCPR is also dominated by strong southerly wind  
316 anomalies (Fig. 3b). In contrast, the south China sea and Philippine sea are covered by  
317 an anomalous cyclone, together with northerly wind anomalies over southern China  
318 (Fig. 3b). Moreover, an anticyclonic anomaly occurs around the Russian Far East,  
319 accompanied by westerly wind anomalies to the north of Japan (Fig. 3b). In the  
320 following spring, the pronounced anticyclonic anomaly over northeast Asia and  
321 associated southerly wind anomalies over the NCPR are replaced by a marked  
322 cyclonic anomaly and northerly wind anomalies (Fig. 3d).



323 Hence, there appears prominent difference in the atmospheric anomalies over  
324 northeast Asia between the persistent and reverse years. Specifically, in the persistent  
325 years, the anomalous anticyclone over northeast Asia and southerly wind anomalies  
326 over NCPR are maintained from winter to following spring. By contrast, in the  
327 reverse years, the wintertime anticyclonic anomaly is replaced by a cyclonic anomaly  
328 over northeast Asia, accompanied by reversal of meridional wind anomalies over  
329 NCPR from winter to the succedent spring.



330  
331 **Figure 4.** Composite anomalies of 850-hPa wind speed (unit:  $\text{m s}^{-1}$ ) in (a, b) winter  
332 and (c, d) spring in the (left column) persistent years and the (right column) reverse  
333 years. Stippling regions indicate anomalies that are statistically significant at the 5%  
334 level.



335

336 **Figure 5.** Composite anomalies of 850-hPa relative humidity (unit: %) in (a, b) winter  
337 and (c, d) spring in the (left column) persistent years and the (right column) reverse  
338 years. Stippling regions indicate anomalies that are statistically significant at the 5%  
339 level.

340 The atmospheric anomalies can impact haze pollution over NCPR in winter and  
341 spring via modulating surface wind speed and relative humidity (e.g. Hang et al. 2013;  
342 Chen et al. 2019, 2020; He et al. 2019; Dang and Liao 2019; Li et al. 2020). The  
343 increase (decrease) in the surface wind speed is (not) conducive to horizontal  
344 diffusion of pollutants, thus contributing to below (above) normal DECC and less  
345 (more) serious haze pollution (Chen et al. 2019; Li et al. 2020). Additionally, large



346 (small) relative humidity is (not) conducive to the generation of secondary organic  
347 compounds and secondary aerosol species (such as  $\text{SO}_4^{2-}$  and  $\text{NO}_3^-$ ), which contribute  
348 to more (less) serious haze pollution over NCPR (Yu et al. 2005; Hennigan et al. 2008;  
349 Chen et al. 2019; Li et al. 2020; Ma and Zhang 2020).

350 Composite anomalies of low-level (850-hPa) wind speed and relative humidity in  
351 winter and spring are shown in Fig. 4 and Fig. 5, respectively. In winter, low-level  
352 wind speed is significantly decreased over the NCPR with a northwestward extension  
353 to the Lake Baikal and an eastward extension to western North Pacific for both the  
354 persistent and reverse years (Figs. 4a and 4b). The southerly wind anomalies to the  
355 western side of the anticyclonic anomaly over northeast Asia (Figs. 3a and 3b) as  
356 opposite to the climatological northerly winds dominated by East Asian winter  
357 monsoon (not shown), lead to decreases in the total wind speed (Figs. 4a and 4b),  
358 which contributes to more serious haze pollution (Figs. 2a and 2b). In addition,  
359 southerly winds anomalies tend to bring more water vapor northward from Southern  
360 Ocean and result in an increase in the relative humidity (Fig. 5a and 5b), which are  
361 also conducive to formation of secondary aerosol species (Yu et al. 2005; Hennigan et  
362 al. 2008; Chen et al. 2019) and contribute to more serious haze pollution over NCPR  
363 in winter (Figs. 2a and 2b). In the persistent years, sustenance of the anticyclonic  
364 anomaly over northeast Asia and southerly wind anomalies over NCPR to the  
365 following spring (Fig. 3c) contributes to above normal DECC in spring (Fig. 2c) via  
366 reducing surface wind speed (Fig. 4c) and increasing relative humidity (Fig. 5c). By  
367 contrast, in the reverse years, reversal of atmospheric anomalies over northeast Asia

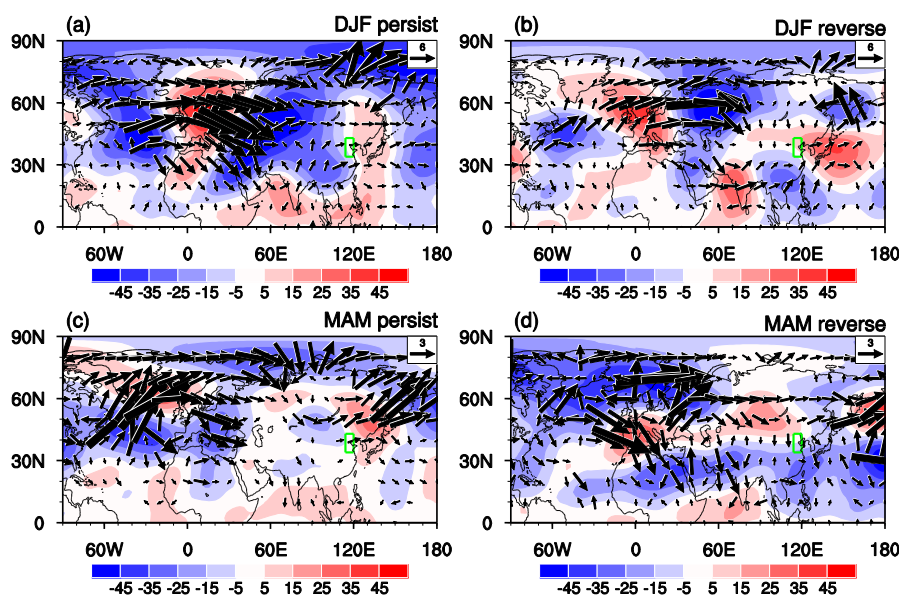


368 from anticyclonic anomaly in winter (Fig. 3b) to cyclonic anomaly in the following  
369 spring (Fig. 3d) results in the inverted DECC anomalies over NCPR (Figs. 2b and 2d).  
370 In spring, the northerly wind anomalies increase the low-level total wind speed (Fig.  
371 4d), which are conducive to the horizontal dispersion of pollutants and contribute to a  
372 better air condition. Additionally, the anomalous northerly winds (Fig. 3d) lead to  
373 decrease in the relative humidity (Fig. 5d) via carrying colder and drier air from  
374 higher latitude, suppressing generation of secondary organic compounds and  
375 secondary aerosol species, and also contributing to mitigation of haze pollution (Fig.  
376 2d). Above evidences suggest that the distinct evolutions of haze pollution over  
377 NCPR between the persistent and reverse years are closely related to the different  
378 evolutions of atmospheric anomalies over northeast Asia.

379 Atmospheric anomalies over northeast Asia related to interannual variations of  
380 haze pollution over NCPR are closely associated with upstream atmospheric wave  
381 train over North Atlantic and mid-high latitudes Eurasia. Studies have demonstrated  
382 that atmospheric wave trains originated from North Atlantic across Eurasia to East  
383 Asia have a strong contribution to interannual variations of haze pollution and climate  
384 anomalies over North China (Yin and Wang 2016, 2017; Zhao et al. 2019; Chen et al.  
385 2019, 2020). Composite anomalies of geopotential height at 500-hPa over larger areas  
386 in winter and succedent spring for the persistent and reverse years are presented in Fig.  
387 6. To examine the possible sources of the atmospheric wave trains over Eurasia, we  
388 also present the wave activity fluxes in Fig. 6, which describe propagation directions  
389 of the atmospheric Rossby waves. Spatial structures of the geopotential height



390 anomalies at 850-hPa and 200-hPa (not shown) are highly similar to those at 500-hPa  
391 in Fig. 6, indicating a vertically barotropic structure of the atmospheric anomalies  
392 over mid-high latitudes of North Atlantic and Eurasia.



393  
394 **Figure 6.** Composite anomalies of 500-hPa geopotential height (shadings, unit: m)  
395 and wave activity fluxes (vectors; unit:  $\text{m}^2 \text{s}^{-2}$ ) in (a, b) winter and (c, d) spring in the  
396 (left column) persistent years and the (right column) reverse years.

397 In the persistent years, an EAWR-like teleconnection pattern is obviously  
398 observed extending from North Atlantic across Europe to East Asia, with negative  
399 geopotential height anomalies (corresponding to cyclonic anomalies) over mid-high  
400 latitudes North Atlantic and central Eurasia, and positive geopotential height  
401 anomalies (corresponding to anticyclonic anomalies) over west Europe and northeast  
402 Asia (Fig. 6a). The pattern correlation coefficient between the EAWR-related 500-hPa  
403 geopotential height anomalies and those in Fig. 6a over the North Atlantic and  
404 Eurasian regions (i.e.  $20^\circ\text{--}90^\circ\text{N}$  and  $70^\circ\text{W}\text{--}130^\circ\text{E}$ ) reaches 0.65, significant at the



405 99.9% confidence level. Hence, in the persistent years, the EAWR teleconnection  
406 contributes largely to the formation of the anticyclonic anomaly over northeast Asia in  
407 winter. In the reverse years, spatial structure of the 500-hPa geopotential height  
408 anomalies over mid-high latitudes of North Atlantic and Eurasia (Fig. 6b) bears a  
409 close resemblance to that for the persistent years (Fig. 6a), also resembles the EAWR  
410 teleconnection pattern. We have also calculated the pattern correlation coefficient  
411 between the 500-hPa geopotential height anomalies in Fig. 6b and those related to the  
412 winter EAWR over the similar region of 20°–90°N and 70°W–130°E. The pattern  
413 correlation coefficient is as high as 0.85, slightly higher than that in the persistent  
414 years ( $r=0.65$ ), suggesting that the EAWR teleconnection pattern also has a strong  
415 contribution to the formation of the wintertime anticyclonic anomaly over Northeast  
416 Asia and haze pollution over the NCPR in the reverse years. Above results are  
417 consistent with Yin and Wang (2017) and Chen et al. (2020). Yin and Wang (2017)  
418 demonstrated that the EAWR teleconnection is the most important atmospheric wave  
419 train modulating haze pollution over North China. Chen et al. (2020) reported that the  
420 winter EAWR teleconnection have a stable and strong impact on the interannual  
421 variation of haze pollution over the NCPR via calculating the running correlation  
422 coefficients between the winter EAWR index and NDI. Note that there exist several  
423 differences in the spatial structure of the wintertime EAWR teleconnection between  
424 the persistent and reverse years (Figs. 6a and 6b). In particular, the center of negative  
425 geopotential height anomalies over central Eurasia in the persistent years (Fig. 6a) is  
426 stronger and shifts southward compared to that in the reverse years (Fig. 6b). In



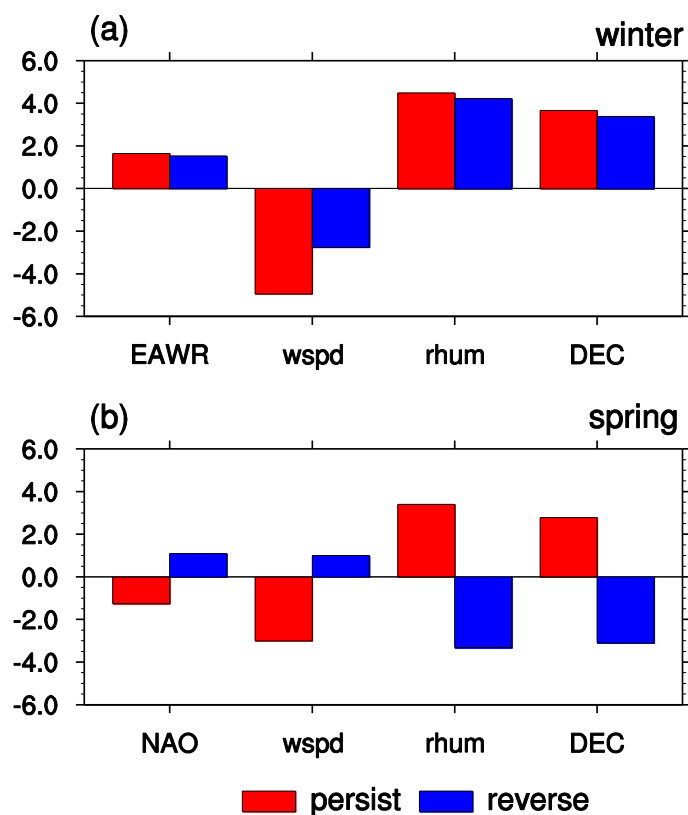
427 addition, negative geopotential height anomalies over western North Atlantic extend  
428 more southwestward for the reverse years (Figs. 6a and 6b). Differences in the spatial  
429 structure of the winter EAWR between the persistent and reverse years may be partly  
430 due to differences in the background mean circulation (Chen and Wu 2017; Wang et al.  
431 2019). Detailed investigation of the factors for the changes of the spatial pattern of the  
432 winter EAWR is out of the scope of this study. Furthermore, it is interesting to note  
433 that an atmospheric Rossby wave exists over subtropical region propagating along the  
434 subtropical Jet stream to extend from north Africa across south Asia and then turn  
435 northeastward to northeast Asia in the reverse years (Fig. 6b). This subtropical wave  
436 train also has a contribution to the formation of the anticyclonic anomaly over  
437 Northeast Asia and interannual variation of haze pollution over the NCPR as has been  
438 indicated by Chen et al. (2020).

439 In spring, a negative NAO-like pattern appears over North Atlantic in the  
440 persistent years, featured by negative geopotential height anomalies around 40°-50°N  
441 and positive anomalies over 60°-70°N in the persistent years (Fig. 6c). The pattern  
442 correlation coefficient between the spring NAO-related 500-hPa geopotential height  
443 anomalies and the composited 500-hPa geopotential height anomalies in Fig. 6c over  
444 North Atlantic region (30°-80°N and 20°W-60°W) is as high as -0.75. This result is  
445 consistent with Chen et al. (2019), which indicated that negative (positive) phase of  
446 the spring NAO contributes to formation of an anomalous anticyclone (cyclone) over  
447 Northeast Asia and leads to more (less) serious haze pollution over NCPR via  
448 eastward propagating wave train. However, in the reverse years, there exists a positive





449 NAO-like pattern over the North Atlantic (Fig. 6d), which is in sharp contrast to that  
450 in the persistent years (Fig. 6c). In particular, the pattern correlation between the  
451 500-hPa geopotential height anomalies in Fig. 6c and spring NAO-related anomalies  
452 over 30°–80°N and 20°W–60°W reaches 0.6. As indicated by Chen et al. (2019), the  
453 spring positive NAO would contribute to below-normal DECC over the NCPR.



454  
455 **Figure 7.** (a) Composite anomalies of the EAWR index, wind speed at 850-hPa ( $4^{-1}$  m  
456  $s^{-1}$ ), relative humidity at 850-hPa (%), and DECC ( $10^{-2}$   $km^{-1}$ ) averaged over NCPR in  
457 winter for the persistent years (red bars) and the reverse years (blue bars). (b)  
458 Composite anomalies of the NAO index, wind speed at 850-hPa ( $m s^{-1}$ ), relative  
459 humidity at 850-hPa (%), and DECC ( $km^{-1}$ ) averaged over NCPR in spring for the  
460 persistent years (red bars) and the reverse years (blue bars).



461 The distinct evolutions of NCPR-average DECC, surface wind speed, relative  
462 humidity, the winter EAWR index, and spring NAO index are summarized in Fig. 7.  
463 In winter, positive phase of the EAWR teleconnection contributes to anticyclonic  
464 anomalies over northeast Asia and associated southerly wind anomalies over the  
465 NCPR, which further leads to positive DECC anomalies both in the persistent and  
466 reverse years via reducing surface wind speed and increasing relative humidity (Fig.  
467 7a). In spring, negative (positive) phase of the spring NAO contributes to formation of  
468 the anomalous anticyclone (cyclone) over northeast Asia, and results in positive  
469 (negative) DECC anomalies over the NCPR via increasing (decreasing) the relative  
470 humidity and decreasing (increasing) the surface wind speed in the persistent (reverse)  
471 years. Above evidences strongly indicate that different evolutions of atmospheric  
472 anomalies over North Atlantic and mid-high latitude Eurasia plays a crucial role in the  
473 distinct evolutions of the haze pollution over NCPR.

474

#### 475 **4. Mechanism for the different evolutions of atmospheric anomalies over North** 476 **Atlantic and Eurasia**

477 What is the possible mechanism for the different evolutions of atmospheric  
478 anomalies over North Atlantic and Eurasia? Considering that the internal atmospheric  
479 process could not explain the connection of the atmospheric anomalies between two  
480 seasons, the evolution of atmospheric anomalies over North Atlantic may be related to  
481 the underlying SSTA. Previous studies have demonstrated that North Atlantic is the  
482 region with strong air-sea interaction (Czaja et al. 2002; Czaja and Frankignoul 2002;

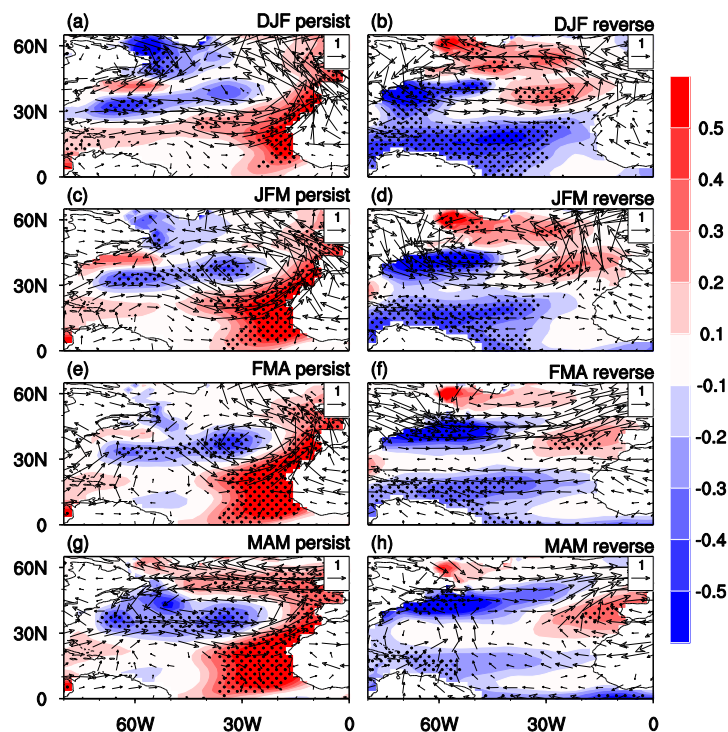


483 Huang and Shukla 2005; Pan 2005; Peng et al. 2003; Wu et al. 2009; Chen et al. 2016,  
484 2018). On one hand, atmospheric anomalies over North Atlantic could lead to SSTA  
485 via modulating surface heat fluxes (Czaja et al. 2002; Huang and Shukla 2005; Wu et  
486 al. 2009; Chen et al. 2015). The connection between the atmospheric anomalies and  
487 SSTA over North Atlantic is closest when atmospheric anomalies lead SSTA by about  
488 one month (Czaja and Frankignoul 2002; Huang and Shukla 2005). On the other hand,  
489 SSTA in the North Atlantic have a strong feedback on the overlying atmospheric  
490 circulation via the heating-induced atmospheric Rossby wave response and the  
491 interaction between low frequency mean flow and synoptic-scale eddy (Peng et al.  
492 2003; Pan 2005; Czaja and Frankignoul 2002; Chen et al. 2020). In particular, a  
493 number of studies have suggested that the development and evolution of atmospheric  
494 anomalies and SSTA over North Atlantic are attributed to the positive air-sea  
495 interaction process there (Czaja and Frankignoul 1999; Rodwell and Folland 2002;  
496 Visbeck et al. 2003; Czaja et al. 2003; Wu and Liu 2005; Hu and Huang 2006; Chen  
497 et al. 2019; Chen et al. 2020).

498 Evolutions of SSTA in the North Atlantic are examined in Fig. 8. In the persistent  
499 years, significant cold SSTA are seen in the central North Atlantic around 30°N and  
500 off the east coast of Canada, together with notable warm SSTA in subtropical eastern  
501 North Atlantic with a northeastward extension to the west coast of Europe (Fig. 8a).  
502 The warm SSTA in the subtropical northeastern Pacific and the cold SSTA in the  
503 central North Atlantic are maintained to the following spring with an increase in the  
504 amplitude. In addition, high latitude North Atlantic is covered by warm SSTA in



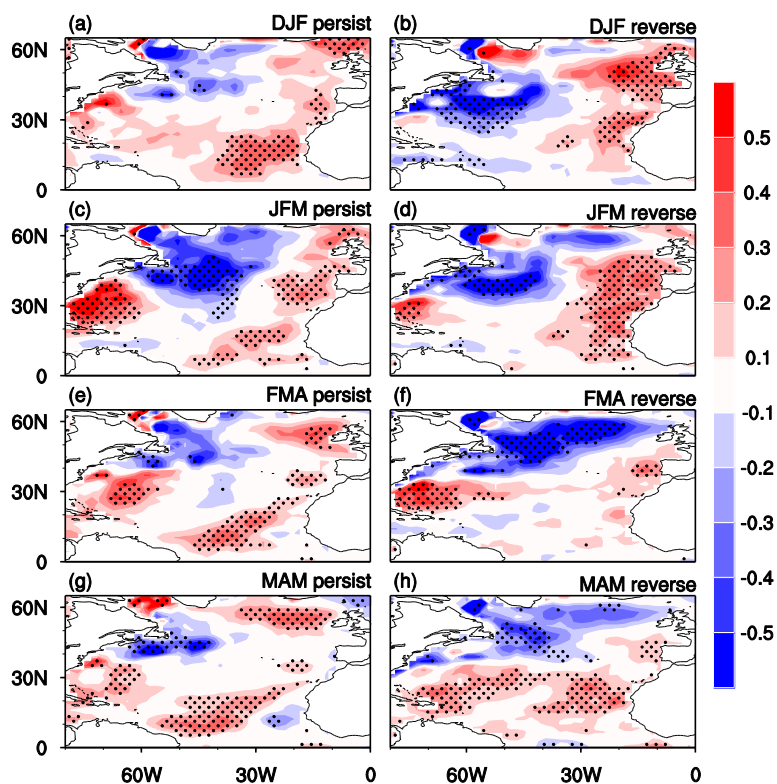
505 spring. This forms a significant tripolar SSTA pattern in spring. Note that the tripolar  
506 SSTA pattern is also the first EOF mode of interannual variation of SSTA in the North  
507 Atlantic (not shown) (Chen et al. 2016, 2020). Studies have demonstrated that warm  
508 (cold) SSTA in the tropical and subtropical North Atlantic related to the tripolar SST  
509 anomaly pattern could induce a negative NAO-like pattern via the Rossby wave type  
510 atmospheric response and wave-mean flow interaction process according to the  
511 observational analysis and numerical experiments (Peng et al. 2003; Pan 2005; Czaja  
512 and Frankignoul 2002; Chen et al. 2016, 2020).



513  
514 **Figure 8.** Composite anomalies of SST ( $^{\circ}\text{C}$ ) and 850-hPa winds ( $\text{m s}^{-1}$ ) in (a, b)  
515 D(0)JF(1), (c, d) JFM(1), (e, f) FMA(1), and (g, h) MAM(1) for (left column) the  
516 persistent years and (right column) the reverse years. Stippling regions in the figure  
517 indicate SST anomalies that are statistically significant at the 5% level.



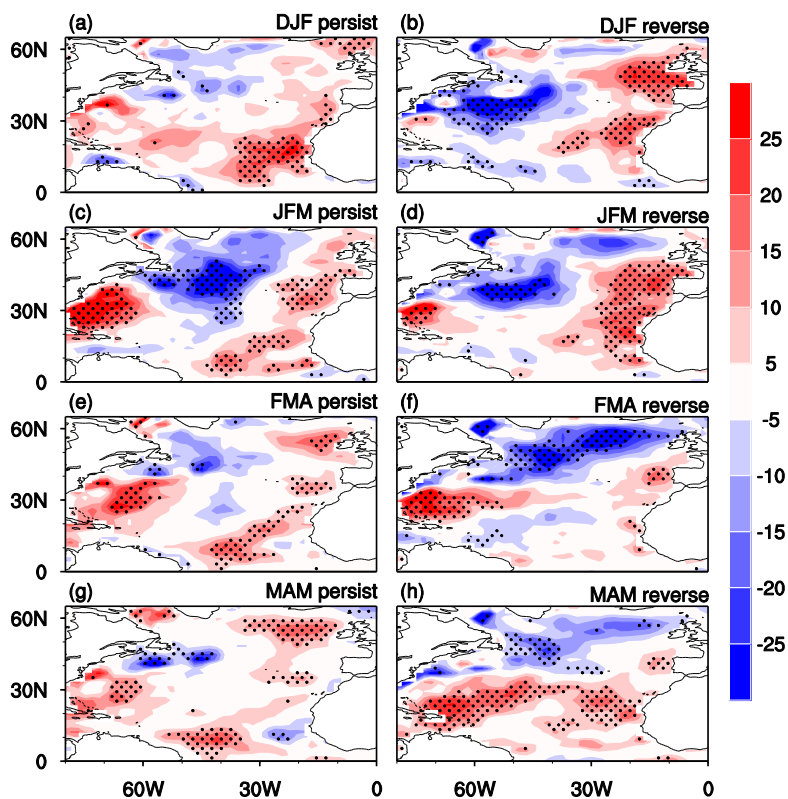
518 In the reverse years, significant cold SSTA are seen in the tropical and  
519 subtropical western North Atlantic in winter (Fig. 8b), which can maintain to  
520 following spring with a decrease in the amplitude (Figs. 8h), which are in sharp  
521 contrast to those in the persistent years (Figs. 8a, c, e, and g). It is reasonable to  
522 speculate that the opposite SSTA in the tropical and subtropical North Atlantic may be  
523 responsible for the opposite atmospheric anomalies over North Atlantic, which will be  
524 confirmed later based on the linear barotropic model.



525  
526 **Figure 9.** Composite anomalies of surface net heat fluxes ( $\text{W m}^{-2}$ ) in (a, b) D(0)JF(1),  
527 (c, d) JFM(1), (e, f) FMA(1), and (g, h) MAM(1) for (left column) the persistent years  
528 and (right column) the reverse years. Stippling regions in the figure indicate  
529 anomalies that are statistically significant at the 5% level.



530 Evolutions of SSTA in the North Atlantic from winter to the following spring are  
531 related to the air-sea interaction. Figure 9 shows composite anomalies of the surface  
532 net heat fluxes for the persistent and reverse years. Values of the surface heat fluxes  
533 have been taken to be positive (negative) when their directions are downward  
534 (upward), which contribute to warm (cold) SSTA. We have also examined composite  
535 anomalies of SST tendency (not shown). It shows that spatial patterns of anomalies of  
536 SST tendency in most parts of North Atlantic are similar to those of the surface net  
537 heat fluxes anomalies. This suggests that changes in the surface net heat fluxes can  
538 largely explain evolutions of SSTA in the North Atlantic from winter to the following  
539 spring. For example, in the persistent years, significant positive net heat flux  
540 anomalies are seen over the subtropical northeastern Atlantic from winter to spring  
541 (Figs. 9a, 9c, 9e, and 9g), which could explain the formation and enhancement of the  
542 positive SSTA there (Figs. 9a, 9c, 9e, and 9g). In addition, the negative surface net  
543 heat flux anomalies to the east of the Canada explain generation and maintenance of  
544 the negative SSTA there. Moreover, the positive surface net heat flux anomalies over  
545 high latitudes contribute to warm SSTA. In the reverse years, positive net heat flux  
546 anomalies appear off the west coast of west Europe (Figs. 9b, d, f, h), which explain  
547 maintenance of the warm SSTA (Figs. 8b, d, f, h). In addition, positive net surface  
548 heat flux anomalies over subtropical western North Atlantic in FMA and MAM (Figs.  
549 9f and 9h) explain the decrease in the amplitude of the negative SSTA there (Figs. 8f  
550 and 8h).



551  
552 **Figure 10.** Composite anomalies of surface latent heat fluxes ( $\text{W m}^{-2}$ ) in (a, b)  
553 D(0)JF(1), (c, d) JFM(1), (e, f) FMA(1), and (g, h) MAM(1) for (left column) the  
554 persistent years and (right column) the reverse years. Stippling regions in the figure  
555 indicate anomalies that are statistically significant at the 5% level.

556 Surface net heat flux anomalies are related to the overlying atmospheric  
557 circulation changes. Surface heat flux consists of four components, including the  
558 surface longwave and shortwave radiations, and surface latent and sensible heat fluxes.  
559 We find that surface net heat flux anomalies (Fig. 10) are dominated by changes in the  
560 surface latent heat flux (Fig. 10). Amplitudes of the surface sensible heat fluxes, and  
561 surface longwave and shortwave radiations are much weaker compared to that of the  
562 surface latent heat flux, and thus are not presented. In the persistent years, the



563 anomalous southwesterly winds over subtropical northeastern Atlantic in winter and  
564 spring oppose the climatological northeasterly winds (Figs. 8a and 8g). This results in  
565 decrease in the total wind speed and decrease in the upward latent heat flux (Figs. 10a  
566 and 10g) and thus contribute to warm SSTA (Figs. 8a and 8g). Note that the warm  
567 SSTA in the subtropical northeastern Atlantic could induce an anomalous cyclone to  
568 its northwestward direction via Rossby wave type atmospheric response (Czaja and  
569 Frankignoul 1999, 2002; Huang and Shukla 2005; Hu and Huang 2006; Chen et al.  
570 2016, 2020) and help maintain the anomalous cyclone over mid-latitude North  
571 Atlantic from winter to spring (Figs. 8a and 8g). Similarly, the anomalous easterly  
572 winds along 60°N over North Atlantic oppose the climatological westerly winds (Figs.  
573 8a and 8g), which lead to warm SSTA there via reduction of wind speed and upward  
574 latent heat fluxes (Figs. 10a and 10g). By contrast, the anomalous northerly winds to  
575 the western flank of the cyclonic anomaly bring colder and drier air from higher  
576 latitude (Figs. 8a and 8g), which increase the upward latent heat flux and contribute to  
577 cold SSTA (Figs. 10a and 10g). In the reverse years, southerly wind anomalies off the  
578 west coast of west Europe carry warmer and wetter air northward from lower latitudes  
579 and lead to warm SSTA (Figs. 8b and 8h) via reduction of upward latent heat flux  
580 (Figs. 10b and 10h). In winter, northerly wind anomalies over the subtropical western  
581 North Atlantic increase the trade wind (Fig. 8b), which result in enhancement of  
582 surface latent heat flux (Fig. 10b) and partly contribute to cold SSTA (Fig. 8b). The  
583 above analyses suggest that evolution of SSTA in the North Atlantic from winter to  
584 subsequent spring is closely related to the air-sea interaction over the North Atlantic.



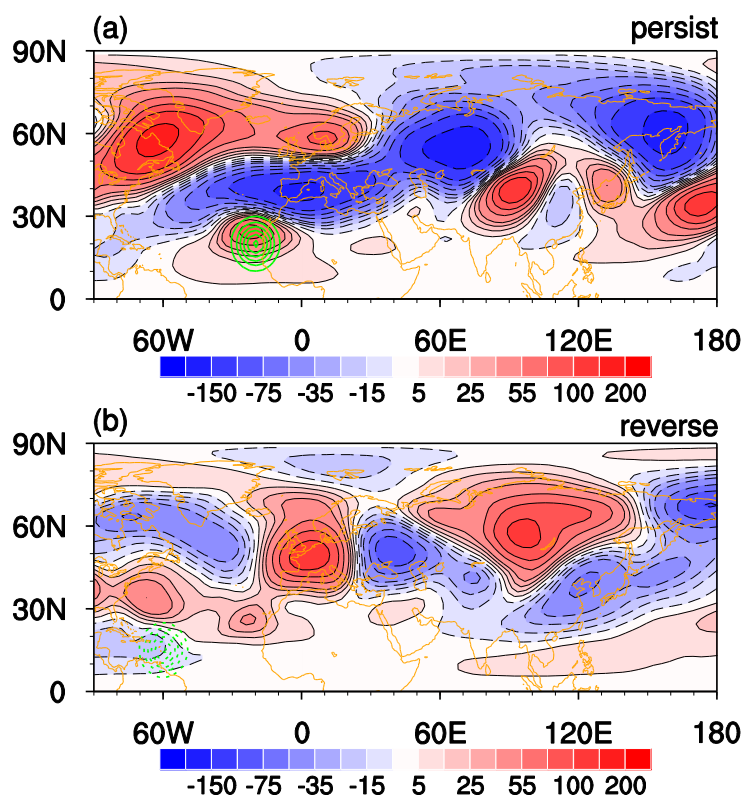


585           The notable differences in the SSTA in the tropical and subtropical North  
586 Atlantic may explain the different atmospheric anomalies over North Atlantic and  
587 Eurasia between the persistent and reverse years, with negative (positive) spring  
588 NAO-like pattern and anticyclonic (cyclonic) anomaly over northeast Asia in the  
589 persistent (reverse) years. Studies have demonstrated that springtime SSTA in the  
590 tropical and subtropical North Atlantic have a strong impact on the atmospheric  
591 circulation and associated climate anomalies over North Atlantic and Eurasia (Wu et  
592 al. 2009; Wu et al. 2011; Chen et al. 2016, 2020). In particular, SSTA in the tropical  
593 and subtropical regions could induce strong vertical motion and atmospheric heating  
594 anomalies reaching to the upper-level troposphere (Ting 1996; Wu et al. 2009;  
595 Hodson et al. 2010; Wu et al. 2011; Sun et al. 2015; Chen et al. 2020). Then, the  
596 divergent/convergent anomalies at the upper-level troposphere induced by the SSTA  
597 could be considered as effective sources for the generation of the atmospheric Rossby  
598 wave (Watanabe 2004; Chen and Huang 2012; Zuo et al. 2013; Chen et al. 2020).  
599 Considering that the atmospheric wave trains extending from the North Atlantic to the  
600 Eurasia in Figs. 6c and 6d resemble an atmospheric stationary Rossby wave with an  
601 equivalent barotropic vertical structure, the mechanism for their formation could be  
602 examined based on the barotropic vorticity equation (Wu et al. 2011; Zuo et al. 2013;  
603 Chen et al. 2016, 2020; O'Reilly et al. 2018). Hence, in the following, we perform  
604 model simulations with barotropic model (Sardeshmukh and Hoskins 1988; Watanabe  
605 2004; O'Reilly et al. 2018) to confirm the possible roles of the spring SSTA in the  
606 North Atlantic in the formation of atmospheric anomalies over the North Atlantic and



607 Eurasia. Studies indicate that the barotropic model has a good performance in  
608 capturing the key dynamics of the atmospheric response to the atmospheric heating  
609 associated with the SSTA in the tropical and subtropical regions (Wu et al. 2011; Sun  
610 et al. 2015; Zuo et al. 2013; Chen et al. 2016, 2020). Three experiments are performed:  
611 the first experiment forced by the spring climatological mean vorticity (denoted as  
612 EXP\_Ctrl); the second experiment forced by the spring climatological mean vorticity  
613 plus the given divergent anomalies over the subtropical northeastern Atlantic with a  
614 center at 20°N, 20°W and maximum intensity of  $7 \times 10^{-6} \times s^{-1}$  according to the spatial  
615 pattern of spring SSTA in Fig. 8g (denoted as EXP\_persist); the third experiment  
616 forced by the spring climatological mean vorticity plus the given convergent  
617 anomalies over the subtropical northwestern Atlantic with a center at 15°N, 60°W and  
618 maximum intensity of  $7 \times 10^{-6} \times s^{-1}$  according to the spatial pattern of spring cold  
619 SSTA in tropical North Atlantic in Fig. 8h (denoted as EXP\_reverse). Above three  
620 experiments are integrated for 40 days. The barotropic model experiments can reach  
621 equilibrium state quickly with only several days (Sardeshmukh and Hoskins 1988;  
622 Zuo et al. 2013; Chen et al. 2016).

623 Figure 11a displays difference of atmospheric responses averaged during model  
624 days 31-40 between EXP\_persist and EXP\_Ctrl with green contours representing the  
625 prescribed divergent anomalies. In addition, difference of the responses between  
626 EXP\_reverse and EXP\_Ctrl is exhibited in Fig. 11b. The barotropic model  
627 experiments can well reproduce the distinct atmospheric anomalies between the  
628 persistent and reverse years.



629  
630 **Figure 11.** (a) Barotropic model height perturbation (unit: m) averaged from days 31  
631 to 40 as a response to the given divergence anomaly (green contours with an interval  
632 of  $10^{-6} \text{ s}^{-1}$ ) over the subtropical eastern North Atlantic with the center at  $20^\circ\text{N}$ ,  $20^\circ\text{W}$ .  
633 (b) Barotropic model height perturbation (unit: m) averaged from days 31 to 40 as a  
634 response to the given convergence anomaly (green contours with an interval of  $10^{-6} \text{ s}^{-1}$ )  
635 over the subtropical western North Atlantic with the center at  $15^\circ\text{N}$ ,  $60^\circ\text{W}$ .

636 In response to the prescribed divergent anomalies over the subtropical  
637 northeastern Atlantic related to the warm SSTA there, there appears a positive  
638 NAO-like pattern with negative geopotential anomalies over mid-latitudes (along  
639  $30^\circ\text{N}$ ) and positive anomalies over high-latitudes (along  $60^\circ\text{N}$ ) North Atlantic  
640 (Fig.11a), largely similar to the spatial pattern of spring atmospheric anomalies in the  
641 persistent years in Fig. 6c. By contrast, in response to the prescribed convergent



642 anomalies over the subtropical northwestern Atlantic associated with the cold SSTA,  
643 there exists a negative NAO-like pattern, with negative geopotential anomalies over  
644 high-latitudes (along 60°N) and negative anomalies over mid-latitudes (along 30°N)  
645 North Atlantic (Fig.11b), in concert with the spatial distribution of the atmospheric  
646 anomalies in the reverse years in Fig. 6d. In addition, it is surprising to see that the  
647 barotropic model experiment well simulate the anticyclonic (cyclone) anomaly over  
648 northeast Asia and related southerly (northerly) wind anomalies over the NCPR in  
649 response to the prescribed forcing in the subtropical northeastern (northwestern)  
650 Atlantic as indicated in Fig. 11a (11b). This is consistent with the observed spring  
651 atmospheric anomalies over East Asia for the persistent (reverse) years, although the  
652 centers of the wave train over Eurasia in the barotropic experiments are not totally  
653 identical to those in the observations. In general, the above barotropic experiments  
654 further confirm the notion that the striking differences in the atmospheric anomalies  
655 over North Atlantic and Eurasia (including northeast Asia) between the persistent and  
656 reverse years can be attributable to the distinct SST anomalies in the North Atlantic.

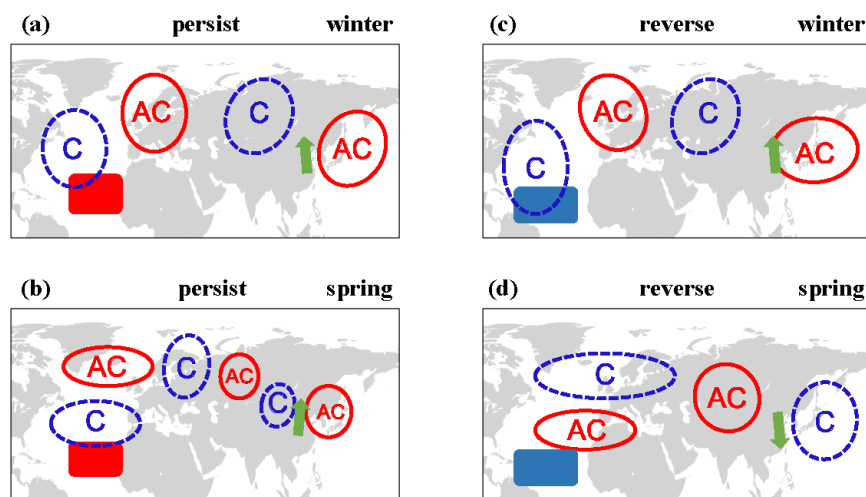
657

## 658 **5. Summary and discussions**

659 This study examines different evolutions of haze pollution over NCPR from  
660 winter to the succedent spring according to the analyses based on observational data  
661 and reanalyses. It is found that interannual variation of haze pollution (as indicated by  
662 the DECC) over NCPR in winter has a marginal positive relation with that in the  
663 following spring, with a correlation coefficient of about 0.3 over 1980–2011 between



664 the haze pollution index in winter and spring, significant at the 90% confidence level.  
665 This indicates that in most years when haze pollution over the NCPR is more (less)  
666 serious in winter, air condition in the following spring is also worse (better) than  
667 normal. Additionally, it is found that there appear some years when DECC anomalies  
668 in the following spring are significantly opposite to those in winter. We then focus on  
669 comparing atmospheric anomalies for the two types of years (i.e. persistent years and  
670 reverse years) to understand why there occur two completely different evolutions of  
671 haze pollution over the NCPR from winter to following spring, as schematically  
672 summarized in Fig. 12.



673  
674 **Figure 12.** Schematic diagram showing evolutions of DECC, SST, and atmospheric  
675 circulation anomalies from winter to spring for (left column) the persistent cases and  
676 (right column) the reverse cases. Red solid contours (blue dashed contours) indicate  
677 anticyclonic circulation anomalies (cyclonic circulation anomalies). Red (blue)  
678 shadings in the North Atlantic indicate positive (negative) SST anomalies.

679 In the persistent years, above-normal DECC (indicating more serious haze  
680 pollution) over the NCPR could be maintained to the succedent spring (Figs. 12a and



681 12b). This is attributable to the persistence of the anticyclonic anomaly over northeast  
682 Asia and associated southerly wind anomalies to its west side over the NCPR (Figs.  
683 12a and 12b). The southerly wind anomalies over the NCPR oppose the  
684 climatological mean northerly winds, reduce the surface wind speed, and decrease the  
685 horizontal dispersion of the pollutants, which finally lead to more serious haze  
686 pollution in winter and spring. In addition, the southerly wind anomalies carry wetter  
687 and warmer air from lower latitude, and lead to increase in the relative humidity,  
688 which are also conducive to haze pollution. As have been demonstrated by previous  
689 studies, the increase in the relative humidity is conducive to the generation of  
690 secondary organic compounds and secondary aerosol species, which also has an  
691 important contribution to the occurrence of haze pollution event over NCPR (Yu et al.  
692 2005; Hennigan et al. 2008). Formation of the anticyclonic anomaly over the  
693 northeast Asia in winter is closely related to the EAWR teleconnection pattern, while  
694 in spring it is related to the positive phase of spring NAO and warm SSTA in the  
695 subtropical northeastern Atlantic (Fig. 12a).

696 In the reverse years, an anticyclonic anomaly also appears over northeast Asia  
697 and associated southerly wind anomalies occur over NCPR in winter, which  
698 contribute to above-normal DECC (Fig. 12c). In addition, formation of the anomalous  
699 anticyclone over the northeast Asia is also related to the EAWR pattern (Fig. 12c).  
700 However, in the following spring, northeast Asia is covered by cyclonic anomaly  
701 which is related to the positive phase of the NAO and cold SSTA in the subtropical  
702 North Atlantic (Fig. 12d), which is in sharp contrast to those in the persistent years.



703 The northerly wind anomalies over the NCPR to the west flank of the anomalous  
704 cyclone result in decrease in the DECC over the NCPR via reduction of relative  
705 humidity and increasing the surface wind speed (Fig. 12d).

706 The distinct evolutions of atmospheric anomalies over North Atlantic and  
707 Eurasia (including northeast Asia) are found to be closely related to the different  
708 evolutions of SSTA in the North Atlantic. In the persistent (reverse) years, positive  
709 (negative) SSTA in the subtropical northeastern (northwestern) Atlantic are  
710 maintained to the following spring due to the positive air-sea interaction process.  
711 Then, positive (negative) spring SSTA in the subtropical North Atlantic contribute to  
712 the formation of negative (positive) NAO-like pattern over North Atlantic and the  
713 generation of anticyclonic (cyclonic) anomaly over northeast Asia, and the occurrence  
714 of associated southerly (northerly) wind anomalies over the NCPR via atmospheric  
715 Rossby wave train. Results of barotropic model simulations with three experiments  
716 further confirm the observed findings.

717 In this study, we find that negative SSTA in the subtropical northwestern Atlantic  
718 play an important role for the formation of the positive NAO-like atmospheric  
719 anomaly in the reverse years. It seems that wintertime surface heat flux changes  
720 induced by the EAWR-related atmospheric anomalies cannot fully explain the  
721 formation of strong cold SSTA in the subtropical northwestern Atlantic. This suggests  
722 that other factors may also be important for the formation of the negative SST  
723 anomalies, which remain to be explored. Studies indicated that ENSO-related SSTA in  
724 the tropical Pacific also has a strong impact on atmospheric anomalies over East Asia



725 and haze pollution over eastern China (Wang et al. 2000; Li et al. 2017; Zhang et al.  
726 2017; He et al. 2019). We have examined evolutions of SSTA in the tropical Pacific  
727 from winter to subsequent spring in the persistent and reverse years. Results show that  
728 SSTA in the tropical Pacific related to ENSO are weak both in the persistent and  
729 reverse years (not shown). This suggests that ENSO-related SSTA may not have a  
730 contribution to the interannual variation of haze pollution over the NCPR, which is  
731 consistent with a recent study by He et al. (2019). It is reported that ENSO-related  
732 SSTA in the tropical Pacific has a significant impact on the haze pollution over  
733 southern China. By contrast, impact of ENSO on the haze pollution over North China  
734 is weak (He et al. 2019). Furthermore, previous studies indicated that Arctic sea ice  
735 and snow cover anomalies over Eurasia may also be important for the formation of  
736 the atmospheric anomalies over East Asia in association with the haze pollution over  
737 north China (Wang et al. 2015; Yin and Wang 2017). Whether snow cover and Arctic  
738 sea changes play a role in contributing to the distinct evolutions of atmospheric  
739 circulation anomalies over Eurasia and haze pollution over NCP remain to be  
740 explored in the future.

741

742 **Code availability.** Figures in this study are constructed with the NCAR Command  
743 Language (<http://www.ncl.ucar.edu/>). All codes used in this study are available from  
744 the corresponding author (S.C.).

745

746 **Data availability:** Atmospheric data are derived from the NCEP-NCAR reanalysis





747 (<http://www.esrl.noaa.gov/psd/data/gridded/data.ncep.reanalysis.html>, last access: 6  
748 February 2021) (NCEP-NCAR, 2021). SST data are obtained from the  
749 <https://psl.noaa.gov/data/gridded/data.noaa.ersst.v5.html> (last access: 6 February 2021)  
750 (NOAA, 2021). Atmospheric teleconnection indices are obtained from  
751 <https://www.cpc.ncep.noaa.gov/data/teledoc/telecontents.shtml> (last access: 6  
752 February 2021) (CPC, 2021). Surface data of visibility and relative humidity can be  
753 obtained from the authors upon request.

754

755 **Author contributions.** Y.L. and C.S. designed the research, performed the analysis  
756 and wrote the paper. All the authors discussed the results and commented on the  
757 manuscript.

758

759 **Competing Interests.** The authors declare that they have no competing interests.

760

761 **Acknowledgments.** This work was supported jointly by the National Natural Science  
762 Foundation of China (Grants 41721004 and 41961144025), and the Chinese Academy  
763 of Sciences Key Research Program of Frontier Sciences (QYZDY-SSW-DQC024).

764

765 **Financial support.** This research has been supported by the National Natural Science  
766 Foundation of China (Grants 41721004 and 41961144025), and the Chinese Academy  
767 of Sciences Key Research Program of Frontier Sciences (QYZDY-SSW-DQC024).

768



769 **References**

- 770 Cohen, A., Brauer, M., Burnett, R., Anderson, H., Frostad, J., Estep, K., Balakrishnan,  
771 K., Brunekreef, B., Dandona, L., Dandona, R., Feigin, V., Freedman, G., Hubbell,  
772 B., Jobling, A., Kan, H., Knibbs, L., Liu, Y., Martin, R., Morawska, L., Pope, C.,  
773 Shin, H., Straif, K., Shaddick, G., Thomas, M., Dingenen, R., Donkelaar, A., Vos,  
774 T., Murray, C., and Forouzanfar, M.: Estimates and 25-year trends of the global  
775 burden of disease attributable to ambient air pollution: An analysis of data from  
776 the Global Burden of Diseases Study 2015, *Lancet*, 389, 1907–1918, 2017.
- 777 Che, H., Zhang, X., Li, Y., Zhou, Z., Qu, J. and Hao, X.: Haze trends over the capital  
778 cities of 31 provinces in China, 1981–2005, *Theor. Appl. Climatol.*, 97, 235–242,  
779 2009.
- 780 Cheng, J., Su, J., Cui, T., Li, X., Dong, X., Sun, F., Yang, Y., Tong, D., Zheng, Y., Li,  
781 Y., Li, J., Zhang, Q., and He, K.: Dominant role of emission reduction in PM<sub>2.5</sub>  
782 air quality improvement in Beijing during 2013–2017: a model-based  
783 decomposition analysis, *Atmos. Chem. Phys.*, 19, 6125–6146, 2019.
- 784 Cai, W.J., Li, K., Liao, H., Wang, H.J. and Wu, L.X.: Weather conditions conducive to  
785 Beijing severe haze more frequent under climate change, *Nat. Clim. Change*, 7,  
786 257–263, 2017.
- 787 Chang, L., Xu, J., Tie, X., and Wu, J.: Impact of the 2015 El Niño event on winter air  
788 quality in China, *Sci. Rep.*, 6, 34275, 2016.
- 789 Craig, C.D. and Faulkenberry, G.D.: The application of ridit analysis to detect trends  
790 in visibility, *Atmos. Environ.*, 13, 1617–1622, 1979.



- 791 Chen, S., Wu, R., and Chen, W.: The changing relationship between interannual  
792 variations of the North Atlantic Oscillation and northern tropical Atlantic SST, *J.*  
793 *Clim.*, 28, 485–504, 2015.
- 794 Chen, S., Wu, R., and Liu, Y.: Dominant modes of interannual variability in Eurasian  
795 surface air temperature during boreal spring, *J. Clim.*, 29, 1109–1125, 2016.
- 796 Chen, S., Guo, J., Song, L., Li, J., Liu, L., and Cohen, J.: Interannual variation of the  
797 spring haze pollution over the North China Plain: Roles of atmospheric  
798 circulation and sea surface temperature, *Int. J. Climatol.*, 39, 783-798, 2019.
- 799 Chen, S., Guo, J., Song, L., Cohen, J., and Wang, Y.: Temporal disparity of the  
800 atmospheric systems contributing to interannual variation of wintertime haze  
801 pollution in the North China Plain, *Int. J. Climatol.*, 40,128-144, 2020.
- 802 Chen, S., Wu, R., Chen, W., and Li, K.: Why does a colder (warmer) winter tend to be  
803 followed by a warmer (cooler) summer over northeast Eurasia? *J. Clim.*, 33,  
804 7255-7274, 2020.
- 805 Czaja, A., and Frankignoul, C.: Influence of the North Atlantic SST on the  
806 atmospheric circulation, *Geophys. Res. Lett.*, 26, 2969–2972, 1999.
- 807 Czaja, A., and Frankignoul, C.: Observed impact of Atlantic SST anomalies on the  
808 North Atlantic oscillation, *J. Climate*, 15, 606–623, 2002.
- 809 Czaja, A., Robertson, A.W., and Huck, T.: The role of Atlantic ocean–atmosphere  
810 coupling in affecting North Atlantic Oscillation variability. *The North Atlantic*  
811 *Oscillation: Climatic Significance and Environmental Impact*, J. W. Hurrell, Eds.,  
812 *Geophys. Monogr.*, Vol. 134, Amer. Geophys. Union, 147–172, 2003.



- 813 Chen, G. S., and Huang, R. H.: Excitation mechanisms of the teleconnection patterns  
814 affecting the July precipitation in Northwest China, *J. Climate*, 25, 7834–7851,  
815 2012.
- 816 CPC: Climate Prediction Center atmospheric teleconnections, available at:  
817 <http://www.esrl.noaa.gov/psd/data/gridded/data.noaa.ersst.v5.html>, last access: 6  
818 February 2021. <https://www.cpc.ncep.noaa.gov/data/teledoc/telecontents.shtml>,  
819 last access: 6 February 2021.
- 820 Ding, Y.H. and Liu, Y.J.: Analysis of long-term variations of fog and haze in China in  
821 recent 50 years and their relations with atmospheric humidity, *Sci. China Earth*  
822 *Sci.*, 57, 36–46, 2014.
- 823 Duan, W., Song, L., Li, Y. and Mao, J. Modulation of PDO on the predictability of the  
824 interannual variability of early summer rainfall over South China, *J. Geophys.*  
825 *Res.*, 118, 1–14, 2013.
- 826 Dang, R., and Liao, H.: Severe winter haze days in the Beijing–Tianjin–Hebei region  
827 from 1985 to 2017 and the roles of anthropogenic emissions and meteorology,  
828 *Atmos. Chem. Phys.*, 19, 10801–10816, 2019.
- 829 Ding, Y., Wu, P., Liu, Y., and Song, Y.: Environmental and dynamic conditions for the  
830 occurrence of persistent haze events in North China, *Engineering* 3, 266–271,  
831 2017.
- 832 Fu, G.Q., Xu, W.Y., Yang, R.F., Li, J.B. and Zhao, C.S.: The distribution and trends of  
833 fog and haze in the North China plain over the past 30 years, *Atmos. Chem.*  
834 *Phys.*, 14, 11949–11958, 2014.



- 835 Gao, H., and Li, X.: Influences of El Niño Southern Oscillation events on haze  
836 frequency in eastern China during boreal winters, *Int. J. Climatol.*, 35, 2682–  
837 2688, 2015.
- 838 Guo, J.P., Su, T., Li, Z., Miao, Y., Li, J., Liu, H., Xu, H., Cribb, M. and Zhai, P.:  
839 Declining frequency of summertime local-scale precipitation over eastern China  
840 from 1970 to 2010 and its potential link to aerosols, *Geophys. Res. Lett.*, 44,  
841 5700–5708, 2017.
- 842 Guo, J., Liu, H., Li, Z., Rosenfeld, D., Jiang, M., Xu, W., Jiang, J. H., He, J., Chen, D.,  
843 Min, M., and Zhai, P.: Aerosol-induced changes in the vertical structure of  
844 precipitation: a perspective of TRMM precipitation radar, *Atmos. Chem. Phys.*,  
845 18, 13329–13343, 2018.
- 846 Hu, Z.-Z., and Huang, B.: On the significance of the relationship between the North  
847 Atlantic Oscillation in early winter and Atlantic sea surface temperature  
848 anomalies, *J. Geophys. Res.*, 111, D12103, 2006.
- 849 Huang, B., and Shukla, J.: Ocean–atmosphere interactions in the tropical and  
850 subtropical Atlantic Ocean. *J. Clim.*, 18, 1652–1672, 2005.
- 851 Hennigan, C.J., Bergin, M.H., Dibb, J.E., and Weber, R.J.: Enhanced secondary  
852 organic aerosol formation due to water uptake by fine particles, *Geophys. Res.*  
853 *Lett.*, 35(18), 2008.
- 854 Hodson, D. L. R., Sutton, R. T., Cassou, C., Keenlyside, N., Okumura, Y., and Zhou,  
855 T. J.: Climate impacts of recent multidecadal changes in Atlantic Ocean sea  
856 surface temperature: A multimodel comparison, *Clim. Dyn.*, 34, 1041–1058,



857           2010.

858   Huang B, and Coauthors.: Extended reconstructed sea surface temperature, version 5  
859           (ERSSTv5): Upgrades, validations, and intercomparisons, *J. Clim.*, 30, 8179–  
860           8205, 2017.

861   Hurrell, J. W.: Decadal trends in the North Atlantic Oscillation. *Science*, 269, 676–679,  
862           195

863   He, C., Liu, R., Wang, X., Liu, S.C., Zhou, T., and Liao, W.: How does El  
864           Niño-Southern Oscillation modulate the interannual variability of winter haze  
865           days over eastern China? *Sci. Total Environ.*, 651, 1892–1902, 2019.

866   Koren, I., Altaratz, O., Remer, L.A., Feingold, G., Martins, J.V. and Heiblum, R. H.:  
867           Aerosol-induced intensification of precipitation from the Tropics to the  
868           mid-latitudes, *Nat. Geosci.*, 5, 118–122, 2012.

869   Kalnay, E., Kanamitsu, M., Kistler, R., Collins, W., Deaven, D., Gandin, L., Iredell,  
870           M., Saha, S., White, G., Woollen, J., Zhu, Y., Leetmaa, A., Reynolds, R.,  
871           Chelliah, M., Ebisuzaki, W., Higgins, W., Janowiak, J., Mo, K.C., Ropelewski,  
872           C., Wang, J., Jenne, R. and Joseph, D.: The NCEP/NCAR 40-year reanalysis  
873           project, *Bull. Amer. Meteor. Soc.*, 77, 437–471, 1996.

874   Koschmieder, H.: Theorie der horizontalen Sichtweite Beit. *Physics of the*  
875           *Atmosphere*, 12, 33–55, 1926.

876   Krishnamurti, T. N., Stefanova, L., and Misra, V.: *Tropical Meteorology: An*  
877           *Introduction*. Springer-Verlag, 424 pp, 2013:

878   Kerr, R.A.: A North Atlantic climate pacemaker for the centuries, *Science*, 288, 1984–



- 879 1986, 2000.
- 880 Li, X., Yu, C., Deng, X., He, D., Zhao, Z., Mo, H., Mo, J., and Wu, Y.: Mechanism for  
881 synoptic and intra-seasonal oscillation of visibility in Beijing-Tianjin-Hebei  
882 region, *Theor. Appl. Climatol.*, 2020.
- 883 Li, J., Li, C. and Zhao, C.: Different trends in extreme and median surface aerosol  
884 extinction coefficients over China inferred from quality-controlled visibility data,  
885 *Atmos. Chem. Phys.*, 18, 3289–3298, 2018.
- 886 Li, Q., Zhang, R. and Wang, Y.: Interannual variation of the wintertime fog-haze days  
887 across central and eastern China and its relation with East Asian winter monsoon,  
888 *Int. J. Climatol.*, 36, 346–354, 2016.
- 889 Liu, T., Gong, S., He, J., Yu, M., Wang, Q., Li, H., et al.: Attributions of  
890 meteorological and emission factors to the 2015 winter severe haze pollution  
891 episodes in China's Jing-Jin-Ji area, *Atmos. Chem. Phys.* 17, 2971–2980, 2017.
- 892 Lu, X., Lin, C., Li, W., Chen, Y., Huang, Y., Fung, J., and Lau, A.: Analysis of the  
893 adverse health effects of PM<sub>2.5</sub> from 2001 to 2017 in China and the role of  
894 urbanization in aggravating the health burden, *Sci. Total Environ.*, 652, 683–695,  
895 2019.
- 896 Li, T., Wang, B., Wu, B., and Zhou, T.: Theories on formation of an anomalous  
897 anticyclone in Western North Pacific during El Niño: a review, *J. Meteorol. Res.*  
898 31, 987–1006, 2017.
- 899 Ma, J., and Zhang, R.: Opposite interdecadal variations of wintertime haze occurrence  
900 over North China Plain and Yangtze River Delta regions in 1980-2013, *Sci. Total*



- 901 Environ., 732, 139240, 2020.
- 902 Mantua, N.J., Hare, S.R., Zhang, Y., Wallace, J.M. and Francis, R.C.: A Pacific  
903 interdecadal climate oscillation with impacts on salmon production, Bull. Amer.  
904 Meteor. Soc., 78, 1069–1079, 1997.
- 905 NCEP-NCAR, Monthly and daily mean atmospheric reanalysis data, available at:  
906 <http://www.esrl.noaa.gov/psd/data/gridded/data.ncep.reanalysis.html>, last access:  
907 6 February 2021.
- 908 NOAA: NOAA Extended Reconstructed Sea Surface Temperature (SST) V5 data sets,  
909 available at: <http://www.esrl.noaa.gov/psd/data/gridded/data.noaa.ersst.v5.html>,  
910 last access: 6 February 2021.
- 911 O'Reilly, C. H., Woollings, T., and Zanna, L.: The impact of tropical precipitation on  
912 summertime Euro-Atlantic circulation via a circumglobal wave train, J. Clim., 31,  
913 6481–6504, 2018.
- 914 Pan, L.-L.: Observed positive feedback between the NAO and the North Atlantic  
915 SSTA tripole, Geophys. Res. Lett., 32, L06707, 2005.
- 916 Peng, S., Robinson, W. A., and Li, S.: Mechanisms for the NAO responses to the  
917 North Atlantic SST tripole, J. Clim., 16, 1987–2004, 2003.
- 918 Rodwell, M. J., and Folland, C. K.: Atlantic air–sea interaction and seasonal  
919 predictability, Quart. J. Roy. Meteor. Soc., 128, 1413–1443, 2002.
- 920 Rosenfeld, D., Dai, J., Yu, X., Yao, Z., Xu, X., Yang, X. and Du, C.: Inverse relations  
921 between amounts of air pollution and orographic precipitation, Science,  
922 315(5817), 1396–1398, 2007.





- 923 Sun, C., Li, J. P., and Zhao, S. Remote influence of Atlantic multidecadal variability  
924 on Siberian warm season precipitation, *Sci. Rep.*, 5, 16853, 2015.
- 925 Sardeshmukh, P. D., and Hoskins, B. J.: The generation of global rotational flow by  
926 steady idealized tropical divergence, *J. Atmos. Sci.*, 45, 1228–1251, 1988.
- 927 Tie, X., Huang, R. and Dai, W.: Effect of heavy haze and aerosol pollution on rice and  
928 wheat productions in China, *Sci. Rep.*, 6, 29612, 2016.
- 929 Takaya, K. and Nakamura, H.: A formulation of a phaseindependent wave activity  
930 flux for stationary and migratory quasigeostrophic eddies on a zonally varying  
931 basic flow, *J. Atmos. Sci.*, 58, 608–627, 2001.
- 932 Ting, M. F.: Steady linear response to tropical heating in barotropic and baroclinic  
933 models, *J. Atmos. Sci.*, 53, 1698–1709, 1996.
- 934 Visbeck, M., Chassignet, E., Curry, R., and Delworth, T.: The ocean's response to  
935 North Atlantic variability. *The North Atlantic Oscillation*, J. Hurrell et al., Eds.,  
936 *Geophys. Monogr.*, Vol. 134, Amer. Geophys. Union, 113–145, 2003.
- 937 Wang, H.J. and Chen, H.P.: Understanding the recent trend of haze pollution in  
938 Eastern China: roles of climate change, *Atmos. Chem. Phys.*, 16, 420–421, 2016.
- 939 Wang, F., Guo, J., Wu, Y., Zhang, X., Deng, M., Li, X., Zhang, J. and Zhao, J.:  
940 Satellite observed aerosol-induced variability in warm cloud properties under  
941 different meteorological conditions over eastern China, *Atmos. Environ.*, 84(2),  
942 122–132, 2014a.
- 943 Wang, Y., Zhang, R. and Saravanan, R.: Asian pollution climatically modulates  
944 mid-latitude cyclones following hierarchical modeling and observational analysis,



- 945 Nature Communications, 5, 3098, 2014b.
- 946 Wu, G., Li, Z.-Q., Fu, C., Zhang, X., Zhang, R.-Y., Zhang, R., Zhou, T., Li, J., Li, J.,  
947 Zhou, D., Wu, L., Zhou, L., He, B., and Huang, R. Advances in studying  
948 interactions between aerosols and monsoon in China, *Sci. China Earth Sci.* 59,  
949 1–16, 2016.
- 950 Wu, Z., Wang, B., Li, J., and Jin, F.-F.: An empirical seasonal prediction model of the  
951 East Asian summer monsoon using ENSO and NAO, *J. Geophys. Res.*, 114,  
952 D18120, 2009.
- 953 Wu, R., Yang, S., Liu, S., Sun, L., Lian, Y., and Gao, Z.: Northeast China summer  
954 temperature and North Atlantic SST, *J. Geophys. Res.*, 116, D16116, 2011.
- 955 Watanabe, M.: Asian jet waveguide and a downstream extension of the North Atlantic  
956 Oscillation, *J. Clim.*, 17, 4674–4691, 2004.
- 957 Wang, L., Liu, Y., Zhang, Y., Chen, W., and Chen, S.: Time-varying structure of the  
958 wintertime Eurasian pattern: Role of the North Atlantic sea surface  
959 temperature and atmospheric mean flow, *Clim Dynam.*, 52, 2467–2479, 2019.
- 960 Wu, L., and Liu, Z.: North Atlantic decadal variability: Air–sea coupling,  
961 oceanic memory, and potential Northern Hemisphere resonance, *J. Clim.*, 18,  
962 331–349, 2005.
- 963 Wang, B., Wu, R.G. and Fu, X.H.: Pacific–East Asian teleconnection: how does  
964 ENSO affect East Asian climate? *J. Clim.*, 13, 1517–1536, 2000.
- 965 Xiao, D., Li, Y., Fan, S., Zhang, R., Sun, J. and Wang, Y.: Plausible influence of  
966 Atlantic Ocean SST anomalies on winter haze in China, *Theor. Appl. Climatol.*,



- 967 122, 249–257, 2014.
- 968 Yin, Z., Wang, H., and Guo, W.: Climatic change features of fog and haze in winter  
969 over North China and Huang-Huai Area, *Sci. China Earth Sci.*, 58, 1370–1376,  
970 2015.
- 971 Yin, Z. and Wang, H.: Role of atmospheric circulations in haze pollution in December  
972 2016, *Atmos. Chem. Phys.*, 17, 11673–11681, 2017.
- 973 Yin, Z. and Wang, H.: The strengthening relationship between Eurasian snow cover  
974 and December haze days in central North China after the mid-1990s, *Atmos.*  
975 *Chem. Phys.*, 18, 4753–4763, 2018.
- 976 Yu, J.Z., Huang, X.F., Xu, J., and Hu, M.: When aerosol sulfate goes up, so does  
977 oxalate: implication for the formation mechanisms of oxalate, *Environ. Sci.*  
978 *Technol.*, 39(1), 128–133, 2005.
- 979 Zhang, Y., Yin, Z., and Wang, H. Roles of climate variability on the rapid increase of  
980 winter haze pollution in north China after 2010, *Atmos. Chem. Phys.*, pp 1–19,  
981 2020.
- 982 Zhang, Y., Wallace, J.M. and Battisti, D.S.: ENSO-like interdecadal variability: 1900–  
983 93, *J. Climate*, 10, 1004–1020, 1997.
- 984 Zhang, J., Liu, J., Ren, L., Wei, J., Duan, J., Zhang, L., Zhou, X., and Sun, Z.: PM<sub>2.5</sub>  
985 induces male reproductive toxicity via mitochondrial dysfunction, DNA damage  
986 and RIPK1 mediated apoptotic signaling pathway, *Sci. Total Environ.*, 634,  
987 1435–1444, 2018.
- 988 Zhang, Q. and Crooks, R.: Toward an environmentally sustainable future: Country



- 989 environmental analysis of the People's Republic of China, China Financial and  
990 Economic Publishing House, Beijing, 2012.
- 991 Zhang, R.H., Min, Q.Y. and Su, J.Z. Impact of El Niño on atmospheric circulations  
992 over East Asia and rainfall in China: role of the anomalous western North Pacific  
993 anticyclone, *Sci. China Earth Sci.*, 60, 1124–1132, 2017.
- 994 Zhang, X., Huang, Y., Zhu, W., and Rao, R. Aerosol characteristics during summer  
995 haze episodes from different source regions over the coast city of North China  
996 Plain, *J. Quant. Spectrosc. Radiat. Transf.*, 122, 180–193, 2013.
- 997 Zhao, S., Li, J., and Sun, C.: Decadal variability in the occurrence of wintertime haze  
998 in central eastern China tied to the Pacific Decadal Oscillation, *Sci. Rep.*, 6,  
999 27424, <https://doi.org/10.1038/srep27424>, 2016.
- 1000 Zhao, W., Chen, S., Chen, W., Yao, S., Nath, D., and Yu, B.: Interannual variations of  
1001 the rainy season withdrawal of the monsoon transitional zone in China, *Clim.*  
1002 *Dynam.*, 53, 2031–2046, 2019.
- 1003 Zuo, J., Li, W., Sun, C., Xu, L., and Ren, H.: Impact of the North Atlantic sea surface  
1004 temperature tripole on the East Asian summer monsoon, *Adv. Atmos. Sci.*, 30,  
1005 1173–1186, 2013.
- 1006